1

General Introduction

1.1 Introduction

According to statistics from the US Energy Information Administration, electrical machines accounted for 43%–46% of the global electricity consumption in 2020 [1] and played an important role in industries and economics. Electrical machines have different types, e.g., direct current (dc) machines, induction machines, reluctance machines, and permanent magnet (PM) machines. Due to their high torque density and efficiency, permanent magnet synchronous machines (PMSMs) have been widely used in various applications, e.g., aerospace, electric vehicles (EVs), industrial drives, servo drives including robots and automation systems, domestic appliances, and wind power generation.

Accurate parameter estimation of PMSMs, including electrical and mechanical parameters, i.e., stator resistance, inductances, rotor flux linkage, and system inertia, is essential for determining the machine characteristics [2–4], improving general control performance [5–8], sensorless control [9–13], and thermal condition monitoring [14–18] for preventing potential irreversible demagnetization of PMs and damage of winding insulation and further improving torque density, as well as fault diagnosis, etc. For example, in EV applications, accurate electrical parameters are required for determining the machine saliency, the reluctance torque, the base speed, the maximum operating speed, the optimal current trajectories under maximum torque per ampere, and maximum power per voltage strategies. For the most common control methods, i.e., field-oriented control (FOC), direct torque control (DTC), as well as model predictive control (MPC), the accurate PMSM parameters are critical to ensuring system stability and improving efficiency and dynamic response. The mechanical parameters, e.g., moment of inertia and viscous friction coefficients, vary significantly with mechanical loads and are important in the design of speed-loop controllers.

Traditionally, the parameters are determined by static open-circuit and short-circuit tests and/or finite element methods. They have significant disadvantages: (a) the machine dimensions and material parameters should be pre-known, (b) there is a rank deficiency issue in most online parameter estimation techniques, (c) parameters are obtained under different operation conditions with conflicts, and (d) variations in speed and load cannot be tracked accurately, which will result in significant errors accounting for magnetic saturation and cross-coupling effect, etc.

In the last few decades, the techniques of parameter estimation have been extensively developed and the parameter estimation can be implemented both offline and online. Generally, offline parameter estimation is essential both in the machine and controller design and has been widely used and investigated [19], in which various computational methods can be employed, i.e., finite element analysis (FEA) and numerical, observer-, and artificial intelligence (AI)-based methods.

Parameter Estimation of Permanent Magnet Synchronous Machines, First Edition. Zi Qiang Zhu, Kan Liu, and Dawei Liang.

However, changes in operation conditions, temperature, mechanical stress, and other environmental factors may cause parameter variations in electrical machines, particularly PMSMs. These variations could result in deteriorated performance, reduced efficiency, and potential damage to the machine over time. To address these challenges, online parameter estimation techniques aim to acquire electrical, mechanical, or thermal parameters under real-time conditions using data gathered during the machine operation [19]. These techniques allow for the continuous monitoring and adjustment of the machine parameters, ensuring that the control system can adapt to changing conditions to maintain optimal performance, and monitoring that the winding and PM temperature cannot exceed the maximum allowable values. Indeed, many commercial industrial drives for PMSMs have embodied the features of parameter estimation functions to ensure efficient and reliable operation.

This book provides a comprehensive resource on basic and state-of-the-art online and offline parameter estimation techniques for PMSMs, including various new online parameter estimation techniques developed at the University of Sheffield and those developed globally, as well as modern control theory–based parameter estimation techniques, with examples of both experimental and simulation results. It addresses the issues of rank deficiency and inverter non-linearity and reports various new online electrical and mechanical parameter estimation techniques for PMSMs, including those with the aid of thermocouples in stator windings, based on current/voltage injection and position offset injection, under constant or variable speed and load for sensored or sensorless controlled PMSMs, accounting for magnetic saturation, cross-coupling, inverter non-linearity, temperature effects, etc. Various applications of parameter estimation techniques of PMSMs for electric vehicles, wind power generators, aerospace, industrial drives, automation systems, robots, and domestic appliances are also reported for improving control performance and sensorless operation, condition monitoring/fault diagnosis, etc.

This chapter briefly describes PMSMs and drives and introduces mathematical models, machine parameters, and parameter estimation techniques accounting for the influence of magnetic saturation and temperature on parameters.

1.2 Permanent Magnet Machines

A typical electrical drive system for PMSMs mainly consists of an electrical machine, a power converter, a load, a rotor position sensor, and a control unit with an employed control strategy. A schematic diagram of a PMSM drive system is shown in Figure 1.1 and will be described in more detail in Section 1.4.

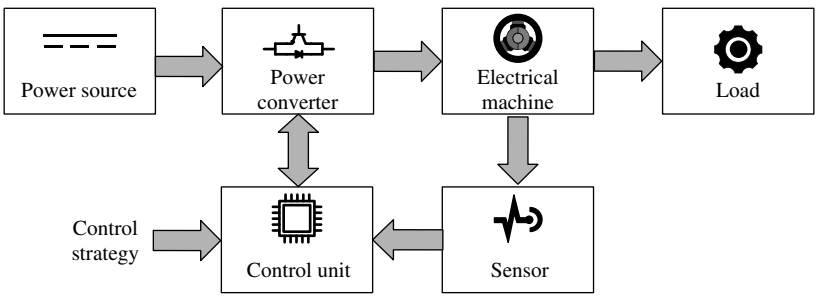

Figure 1.1 Schematic diagram of PMSM drive system.

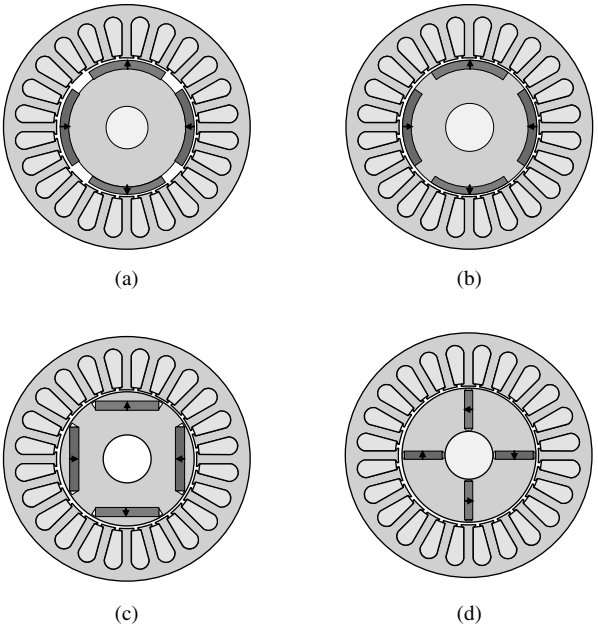

Figure 1.2 Machine configurations of radial-flux internal rotor PMSMs: (a) surface-mounted PM, (b) surface-inset PM, (c) I-type interior PM (radially magnetized), and (d) spoke-type interior PM (circumferentially magnetized).

In most PMSMs, PMs are usually located on the rotor for excitation. According to the directions of the magnetic flux in the air gap, the majority of PMSMs can be categorized into radial and axial flux machines, of which radial-flux rotor PM machines are the most common in terms of electromagnetic performance, manufacturability, cost, etc. The radial-flux rotor PM machines have either an internal or external rotor, while the PMs could be assembled either on the surface or in the interior of the rotor, as shown in Figure 1.2.

In surface-mounted PM (SPM) machines, as shown in Figure 1.2a, the PMs are mounted on the rotor surface and are adjacent to the air gap. There is negligible magnetic saliency and reluctance torque, and PM torque is the major torque component. Since the relative permeability of PMs is almost the same as that of air, the *dq*-axis inductances in SPM machines are almost equal and lower than those of the interior PM (IPM) machines. Furthermore, the field produced by stator windings in SPM machines is low, and hence, the winding inductance is also low. However, SPMs need a rotor sleeve/binding for retaining, particularly in high-speed applications [20]. The sleeve/binding materials can be glass fibre, carbon fibre, or non-magnetic stainless steel. However, in external rotor SPM machines, the rotor back iron can be utilized for retaining PMs. External rotor SPM machines are preferred in high-power low-speed direct-drive wind power generators or hub motors for EVs. Besides, the PM, which can be inset into the rotor surface, as shown in Figure 1.2b, is laterally adjacent to the rotor core. In this case, the magnet pole arc to pole pitch ratio needs to be smaller than one, but PMs can be easily fixed between two adjacent interpole irons. Since the *q*-axis inductance is larger than the *d*-axis inductance, a reluctance torque component exists in inset SPM machines.

In IPM machines, as shown in Figure 1.2c and d, PMs are radially or circumferentially magnetized, respectively. Radially magnetized IPM rotors are more commonly used, e.g., in EV applications, but circumferentially magnetized IPM rotors, i.e., spoke-type IPM rotors, are very popular in domestic appliances since the PM flux focusing effect may be utilized when the pole number is high and cheap ferrite magnets can be used for reducing the cost. Since PMs are embedded in the rotor core, extra rotor PM retaining is not required, but PM leakage fluxes are more significant, and hence, airspace flux barriers are often required next to the iron ribs to reduce the PM leakage flux.

Compared with SPM machines, since the q-axis inductance is usually larger than the d-axis inductance, IPM machines exhibit a high saliency ratio, thereby both PM and reluctance torques can be utilized. Furthermore, the field produced by stator windings in the IPM machines is much higher, leading to higher magnetic saturation in the d- or q-axis and higher cross-coupling between dq-axes [21]. Furthermore, the flux produced by stator windings in radially magnetized IPM machines passes through two PMs, while that in circumferentially magnetized spoke-type machines only passes a single PM. Thus, the spoke-type IPM machines exhibit a higher d-axis inductance.

Besides the I-type IPM machines, there are various other PM configurations as shown in Figure 1.3, including single-/double-layer V-type rotors for utilizing PM flux focusing, double-layer V-type, double-layer I-type, and delta-type rotors for increasing the reluctance torque with higher saliency ratio. These IPM rotor machines have been widely employed in EVs [22, 23]. The main aims for IPM rotor design in EV applications are high performance and low cost, i.e., increased output torque by utilizing the reluctance torque, reduced number and amount of PMs, and ease of manufacturing. Therefore, in practice, the maximum number of layers is usually less than three, with two layers being the most common, since the benefits of employing a layer number higher than three for increasing reluctance torque diminish significantly.

To utilize the reluctance torque, the coil pitch of the stator windings should be as close as possible to the pole pitch of the rotor PMs, and thus, the end windings of different phases will be overlapped, resulting in overlapping windings (Figure 1.4a). Furthermore, to improve the back electromotive force (EMF) waveform and reduce its total harmonic distortion (THD), the rotor PM segments are often step skewed, while distributed overlapping stator windings are often employed. However, overlapping windings have longer end windings, which result in a longer machine axial length and higher copper loss. Non-overlapping stator windings or tooth coils can be utilized to reduce the end winding length and the end winding copper loss in the PM machines, which usually have a fractional slot number per pole per phase, i.e., fractional slot PM machines. In fractional slot PM machines, cogging torque or torque ripple is low, but the reluctance torque will be significantly reduced or even become

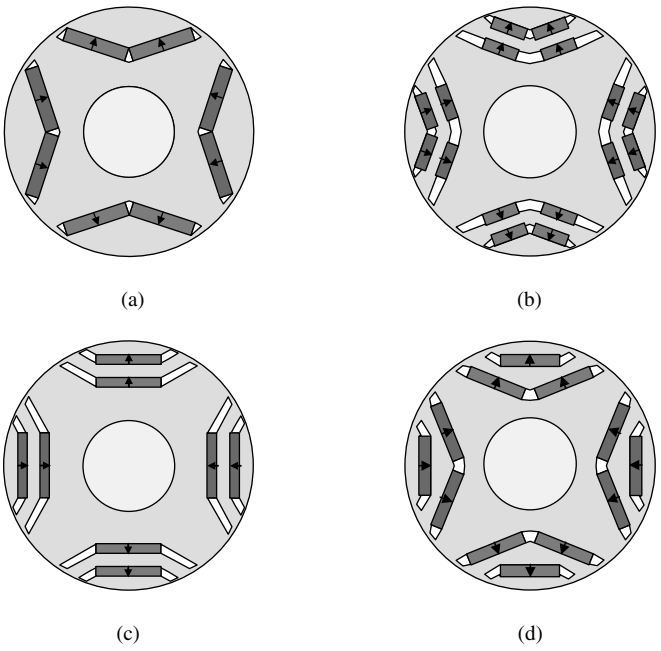

Figure 1.3 Variants of IPM rotor configurations: (a) single V-type, (b) double V-type, (c) double I-type, and (d) delta type.

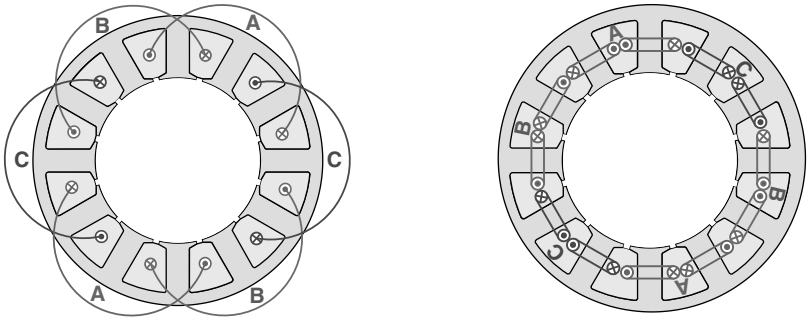

Figure 1.4 Stator winding topologies: (a) overlapping windings (12-slot stator for 4-pole rotor) and (b) non-overlapping windings (12-slot stator for 10-pole rotor).

negligible. Fractional slot PM machines (Figure 1.4b) are often used in domestic appliances and electric-assisted power steering.

1.3 Basic Equations and Machine Parameters

The mathematical modelling of PM machines is essential for control and parameter estimation. This section introduces the fundamental mathematical models of three-phase SPMSM and IPMSM. Meanwhile, the influences of magnetic saturation and temperature on the variation of parameters are also discussed.

1.3.1 Fundamental Mathematical Model for PMSMs

To simplify the mathematical modelling, several assumptions are made as follows:

1. The magnetic saturation, thermal effect, and stator iron loss are ignored.
2. The permeabilities of the PM and the air are the same.
3. The three-phase windings are distributed symmetrically in space. Both the magnetomotive forces (MMFs) generated by the stator windings and the back EMFs in the stator windings induced by the rotor PMs are sinusoidal.

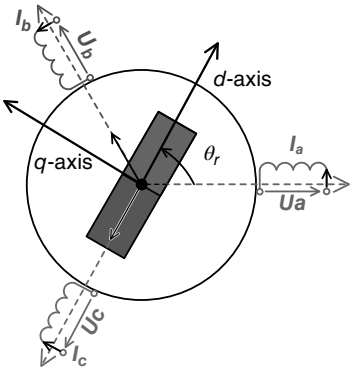

Figure 1.5 Representation of the three-phase PM machine model.

A three-phase PMSM model is presented in Figure 1.5, where $u_{a,b,c}$ can be calculated as follows:

$$\begin{bmatrix} u_a \\ u_b \\ u_c \end{bmatrix} = R_s \begin{bmatrix} i_a \\ i_b \\ i_c \end{bmatrix} + \frac{d}{dt} \begin{bmatrix} \psi_a \\ \psi_b \\ \psi_c \end{bmatrix} \tag{1.1a}$$

$$\begin{bmatrix} \psi_a \\ \psi_b \\ \psi_c \end{bmatrix} = \begin{bmatrix} L_{aa} & L_{ab} & L_{ac} \\ L_{ba} & L_{bb} & L_{bc} \\ L_{ca} & L_{cb} & L_{cc} \end{bmatrix} \begin{bmatrix} i_a \\ i_b \\ i_c \end{bmatrix} + \psi_{pm} \begin{bmatrix} \cos(\theta_r) \\ \cos(\theta_r - 2\pi/3) \\ \cos(\theta_r + 2\pi/3) \end{bmatrix} \tag{1.1b}$$

where R_s is the stator winding resistance. $i_{a,b,c}$ and $\psi_{a,b,c}$ are the three-phase currents and flux linkages, respectively. ψ_{pm} is the PM flux linkage. θ_r is the rotor angular position. L_{ii} and L_{ij} with $\{i,\ j = a,b,c\}$ are the self- and mutual-inductances, respectively.

For SPM machines, the self- and mutual-inductances are constant as shown in Eq. (1.2) due to the assumed uniform air gap permeance [24]:

$$L_{aa} = L_{bb} = L_{cc} = L_m + L_{s\sigma} \tag{1.2a}$$

$$L_{ab} = L_{ac} = L_{ba} = L_{bc} = L_{ca} = L_{cb} = -\frac{1}{2}L_m \tag{1.2b}$$

where L_m and $L_{s\sigma}$ are the phase self-inductance and the leakage inductance, respectively.

For IPM machines, the self- and mutual-inductances depend on the rotor position due to the saliency of the rotor:

$$\begin{cases} L_{aa} = L_m + L_{s\sigma} + L_{s2}\cos(2\theta_r) \\ L_{bb} = L_m + L_{s\sigma} + L_{s2}\cos(2\theta_r + 2\pi/3) \\ L_{cc} = L_m + L_{s\sigma} + L_{s2}\cos(2\theta_r - 2\pi/3) \end{cases} \tag{1.3a}$$

$$\begin{cases} L_{ab} = L_{ba} = M_{s0} + M_{s2}\cos(2\theta_r - 2\pi/3) \\ L_{bc} = L_{cb} = M_{s0} + M_{s2}\cos(2\theta_r) \\ L_{ac} = L_{ca} = M_{s0} + M_{s2}\cos(2\theta_r + 2\pi/3) \end{cases} \tag{1.3b}$$

where L_{s2} is the amplitude of the second-order harmonic of self-inductances. M_{s0} and M_{s2} are the average value and amplitude of the second-order harmonic of mutual-inductances, respectively.

By using the Clarke transformation $\mathbf{T}_{abc-\alpha\beta0}$ in Eq. (1.4), the three-phase voltage equations (Eq. 1.1) can be transferred to the stationary $\alpha\beta$-axis, i.e.,

$$\mathbf{T}_{abc-\alpha\beta0} = \frac{2}{3}\begin{bmatrix} 1 & -1/2 & -1/2 \\ 0 & \sqrt{3}/2 & -\sqrt{3}/2 \\ 1/2 & 1/2 & 1/2 \end{bmatrix} \tag{1.4}$$

$$\begin{bmatrix} u_\alpha \\ u_\beta \end{bmatrix} = R_s\begin{bmatrix} i_\alpha \\ i_\beta \end{bmatrix} + \frac{d}{dt}\begin{bmatrix} \psi_\alpha \\ \psi_\beta \end{bmatrix} \tag{1.5a}$$

$$\begin{bmatrix} \psi_\alpha \\ \psi_\beta \end{bmatrix} = \begin{bmatrix} \Sigma L + \Delta L\ \cos(2\theta_r) & \Delta L\ \cos(2\theta_r) \\ \Delta L\ \sin(2\theta_r) & \Sigma L - \Delta L\ \cos(2\theta_r) \end{bmatrix}\begin{bmatrix} i_\alpha \\ i_\beta \end{bmatrix} + \psi_{pm}\begin{bmatrix} \cos(\theta_r) \\ \sin(\theta_r) \end{bmatrix} \tag{1.5b}$$

where $\Sigma L = (L_d + L_q)/2$ and $\Delta L = (L_d - L_q)/2$. L_d and L_q are the inductances in the dq-axes.

Afterward, the Park transformation $\mathbf{T}_{\alpha\beta-dq}$ (Eq. 1.6) is used to transform the stationary $\alpha\beta$-axis system to the rotating dq-axis system, where the rotor position–related terms could be cancelled:

$$\mathbf{T}_{\alpha\beta-dq} = \begin{bmatrix} \cos(\theta_r) & \sin(\theta_r) \\ -\sin(\theta_r) & \cos(\theta_r) \end{bmatrix} \tag{1.6}$$

$$\begin{bmatrix} u_d \\ u_q \end{bmatrix} = R_s\begin{bmatrix} i_d \\ i_q \end{bmatrix} + \frac{d}{dt}\begin{bmatrix} \psi_d \\ \psi_q \end{bmatrix} \tag{1.7a}$$

$$\begin{bmatrix} \psi_d \\ \psi_q \end{bmatrix} = \begin{bmatrix} L_d & 0 \\ 0 & L_q \end{bmatrix}\begin{bmatrix} i_d \\ i_q \end{bmatrix} + \begin{bmatrix} \psi_{pm} \\ 0 \end{bmatrix} \tag{1.7b}$$

where u_d, u_q, i_d, i_q, L_d, and L_q are the dq-axis voltages, currents, and inductances, respectively. The phasor diagram of a PM machine can be derived from Eq. (1.7), as presented in Figure 1.6, where γ and φ are the current advancing angle and the power factor angle, respectively.

Finally, by introducing Eq. (1.7b) into Eq. (1.7a), the voltage equations $u_{d,q}$ can be written as follows:

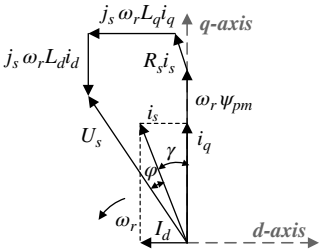

Figure 1.6 Phasor diagram of three-phase PM machine.

$$\begin{cases} u_d = R_s i_d + L_d^{\text{inc}} \dfrac{di_d}{dt} - \omega_r L_q^{\text{ap}} i_q \\ u_q = R_s i_q + L_q^{\text{inc}} \dfrac{di_q}{dt} + \omega_r \left(L_d^{\text{ap}} i_d + \psi_{pm} \right) \end{cases} \tag{1.8}$$

$$L_{d,q}^{\text{inc}} = \frac{d\psi_{d,q}}{di_{d,q}} \tag{1.9a}$$

$$L_{d,q}^{\text{ap}} = \frac{\psi_{d,q}}{i_{d,q}} \tag{1.9b}$$

where $L_{d,q}^{\text{inc}}$ and $L_{d,q}^{\text{ap}}$ are the dq-axis incremental and apparent inductances, respectively. ω_r is the rotor angular velocity. When the magnetic material is not saturated, i.e., linear, the incremental inductance is the same as the apparent inductance. Otherwise, the incremental inductances become smaller once the magnetic material is saturated due to the non-linear change of the flux linkage with the current, which will be discussed in the next section in detail.

Besides, the electromagnetic torque and the motion equation are expressed as follows:

$$T_e = \frac{3}{2} p \left[\psi_{pm} i_q + \left(L_d - L_q \right) i_d i_q \right] \tag{1.10}$$

$$J \frac{d\omega_r}{dt} = p \left[T_e - T_L - \frac{F}{p} \omega_r \right] \tag{1.11}$$

where p, J, T_L, and F are the number of pole pairs, the rotor moment of inertia, the load torque, and the friction coefficient, respectively.

1.3.2 Mathematical Model Considering Magnetic Saturation, Thermal Effect, and Iron Loss

1.3.2.1 Influence of Magnetic Saturation

As mentioned above, the ideal mathematical model does not consider the magnetic saturation effect. However, in reality, the magnetic materials are less than ideal, i.e., they will be saturated with the increase in current or magnetic flux. Hence, the magnetic permeabilities and the effectiveness in the contribution of overall flux density will be decreased [25]. Consequently, in the parameter estimation, the magnetic saturation significantly affects the flux linkages, and thus, the dq-axis inductances. Accounting for the magnetic saturation, the correlation between the incremental and apparent inductances is illustrated in Figure 1.7.

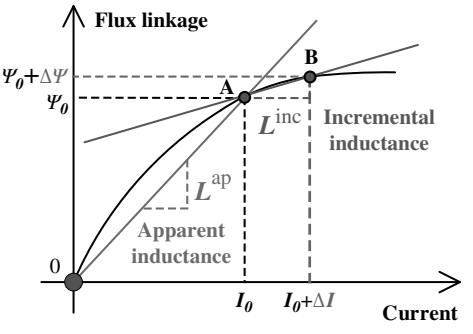

Figure 1.7 Incremental and apparent inductances considering magnetic saturation.

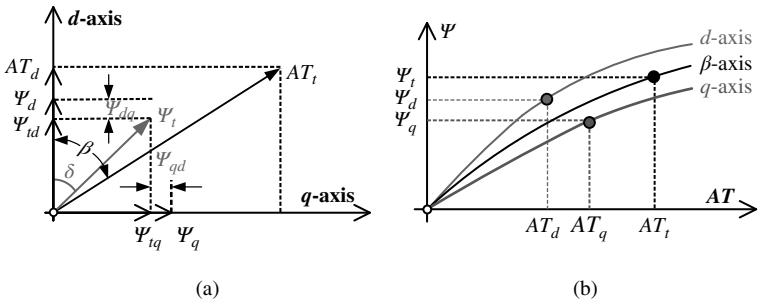

Figure 1.8 Illustration of cross-coupling effect based on a salient-pole synchronous machine: (a) flux vector diagram and (b) saturation curves.

As can be seen, when the magnetic material becomes saturated, both the apparent and incremental inductances will gradually decrease, and the value of incremental inductance will be smaller than the corresponding apparent inductance. Besides the self-saturation, the cross-coupling effect also plays an important role in the electromagnetic performance when the machine is saturated [26, 27], as illustrated in Figure 1.8.

In Figure 1.8a, when the machine is excited by the ampere-turns AT_d and AT_q in the d- and q-axis directions separately, the generated fundamental components of the air gap magnetic fluxes are Y_d and Y_q, respectively. In contrast, when the machine is excited by AT_d and AT_q along the d- and q-axis directions simultaneously, the resultant magnetic flux Y_t corresponding to the total ampere-turns AT_t can be found from the saturation curve (β-axis) in Figure 1.8b. Consequently, the resolved Y_{td} and Y_{tq} are unequal to Y_d and Y_q, respectively. δ is the angle between the total airgap flux and the d-axis when the machine is excited from the d- and q-axis directions simultaneously. The variations of fluxes in the d- and q-axis, Y_{dq} and Y_{qd}, are attributed to the magnetic cross-coupling effect.

Meanwhile, PM flux linkage is also affected by magnetic saturation [28]. Therefore, derived from the ideal equations (Eqs. 1.7 and 1.8), the dq-axis voltage equations and flux linkages accounting for the magnetic saturation effect could be extended and rewritten as follows:

$$\begin{cases} u_d = R_s i_d + L_d^{\text{inc}} \dfrac{di_d}{dt} + L_{dq}^{\text{inc}} \dfrac{di_q}{dt} - \omega_r \psi_q \\ u_q = R_s i_q + L_q^{\text{inc}} \dfrac{di_q}{dt} + L_{qd}^{\text{inc}} \dfrac{di_d}{dt} + \omega_r \psi_q \end{cases} \tag{1.12a}$$

$$\begin{bmatrix} \psi_d \\ \psi_q \end{bmatrix} = \begin{bmatrix} L_d(i_d, i_q) & L_{dq}(i_d, i_q) \\ L_{qd}(i_d, i_q) & L_q(i_d, i_q) \end{bmatrix} \begin{bmatrix} i_d \\ i_q \end{bmatrix} + \begin{bmatrix} \psi_{pm}(i_d, i_q) \\ 0 \end{bmatrix} \tag{1.12b}$$

where L_{dq}, L_{qd}, L_{dq}^{inc}, and L_{qd}^{inc} are the dq-axis apparent and incremental mutual inductances, respectively. The relationship between the incremental and apparent inductance can be found in Ref. [29], where the dq-axis incremental inductance matrix $\boldsymbol{L}_{\boldsymbol{dq}}^{\mathbf{inc}}$ is adjusted to the diagonal matrix $\boldsymbol{L}_{\boldsymbol{dq}.\mathbf{adj}}^{\mathbf{inc}}$:

$$\boldsymbol{L}_{\boldsymbol{dq}}^{\mathbf{inc}} = \begin{bmatrix} L_d^{\text{inc}} & L_{dq}^{\text{inc}} \\ L_{qd}^{\text{inc}} & L_q^{\text{inc}} \end{bmatrix} \tag{1.13}$$

$$\boldsymbol{L}_{\boldsymbol{dq}.\mathbf{adj}}^{\mathbf{inc}} = \begin{bmatrix} L_{d,\text{adj}}^{\text{inc}} & 0 \\ 0 & L_{q,\text{adj}}^{\text{inc}} \end{bmatrix} \tag{1.14}$$

where

$$\begin{cases} L_{d,\mathrm{adj}}^{\mathrm{inc}} = \dfrac{L_d^{\mathrm{inc}}\Delta i_d + L_{dq}^{\mathrm{inc}}\Delta i_q}{\Delta i_d} \\ L_{q,\mathrm{adj}}^{\mathrm{inc}} = \dfrac{L_q^{\mathrm{inc}}\Delta i_q + L_{qd}^{\mathrm{inc}}\Delta i_d}{\Delta i_q} \end{cases} \tag{1.15}$$

Thus, the equivalent apparent inductances, L_d^{ap} and L_q^{ap}, can be calculated as follows:

$$\begin{cases} L_d^{\mathrm{ap}} = \dfrac{\int L_{d,\mathrm{adj}}^{\mathrm{inc}}(i_d)\, di_d}{i_d} \\ L_q^{\mathrm{ap}} = \dfrac{\int L_{q,\mathrm{adj}}^{\mathrm{inc}}(i_q)\, di_q}{i_q} \end{cases} \tag{1.16}$$

It is worth mentioning that there is a third type of inductance definition [30–32], which is often called energy inductance.

The energy inductances are derived based on the energy perturbation method and also involve incremental and apparent inductances. In general, the self- and mutual inductances, L_{ii} and L_{ij}, are calculated as follows:

$$L_{ii} = \frac{\partial^2 W}{\partial(\Delta i_i)^2} \tag{1.17a}$$

$$L_{ij} = \frac{\partial^2 W}{\partial(\Delta i_i)\,\partial(\Delta i_j)} \tag{1.17b}$$

where W is the total stored energy and Δi_i and Δi_j are the current perturbations in the ith and jth coils, respectively. For the calculation of apparent inductance, the apparent reluctivity is used to determine the perturbations in energies (excess or deficit), whereas the incremental reluctivity is used to calculate incremental inductance, as presented in Figure 1.9 [30–32].

1.3.2.2 Influence of Temperature

The stator winding resistance and PM flux linkage are also dependent on the temperature. With the rise in the operating temperature, the stator winding resistances will be increased, while the PM flux linkage be decreased:

$$R_{s,s} = R_{s,0}\left[1 + \alpha_{cu}(\vartheta_s - \vartheta_r)\right] \tag{1.18}$$

$$\psi_{pm,s} = \psi_{pm,0}\left[1 + \alpha_{pm}(\vartheta_{pm} - \vartheta_r)\right] \tag{1.19}$$

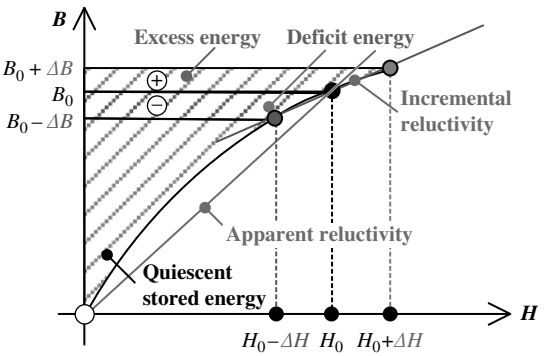

Figure 1.9 Representation of apparent and incremental reluctivities in non-linear magnetic material including energy perturbation.

where $R_{s,s}$, $R_{s,0}$, $\psi_{pm,s}$, and $\psi_{pm,0}$ are the stator winding resistance and the PM flux linkage at the actual average temperatures ϑ_s and ϑ_{pm}, as well as at the reference temperature ϑ_r. α_{cu} and α_{pm} are the temperature coefficients for copper and PM, respectively.

Table 1.1 tabulates the characteristics of typical PM materials, including ferrite, AlNiCo, SmCo, and NdFeB magnet materials, together with their temperature coefficients.

A commercial NdFeB PM material, i.e., N4514 [34], is taken as an example; its intrinsic and normal *BH* curves accounting for different temperatures are presented in Figure 1.10.

As can be seen, the main indicators for the performance assessment of PMs include the remanence B_r, the coercivity H_c, the intrinsic coercivity H_{cl}, and the maximum energy product $BH_{\max}$. Once the external demagnetization field exceeds the knee point, the magnetic flux density

Table 1.1 Physical properties of PM materials.

Parameters	Ferrite	AlNiCo	$SmCo_5$	NdFeB
Remanence B_r (T)	0.38–0.42	0.61–1.35	0.85–1.0	1.0–1.23
Coercivity H_C (kA/m)	280–390	50–59	1000–1200	960–1600
Maximum energy product $BH_{\max}$ (kJ/m^3)	10–40	35–60	150–240	200–480
Temperature coefficient of B_r (%/°C)	−0.2	−0.03	−0.06 to −0.02	−0.15 to −0.1
Temperature coefficient of H_c (%/°C)	0.2 to 0.5	<0.1	−0.4 to −0.2	−0.6 to −0.4
Relative permeability μ_r	1.05	<5	1.05	<1.2
Electrical resistivity ρ_{ele} (Ω·m)	$>10^4$	5×10^{-3}	0.8×10^{-6}	1.5×10^{-6}

Source: Adapted from [33].

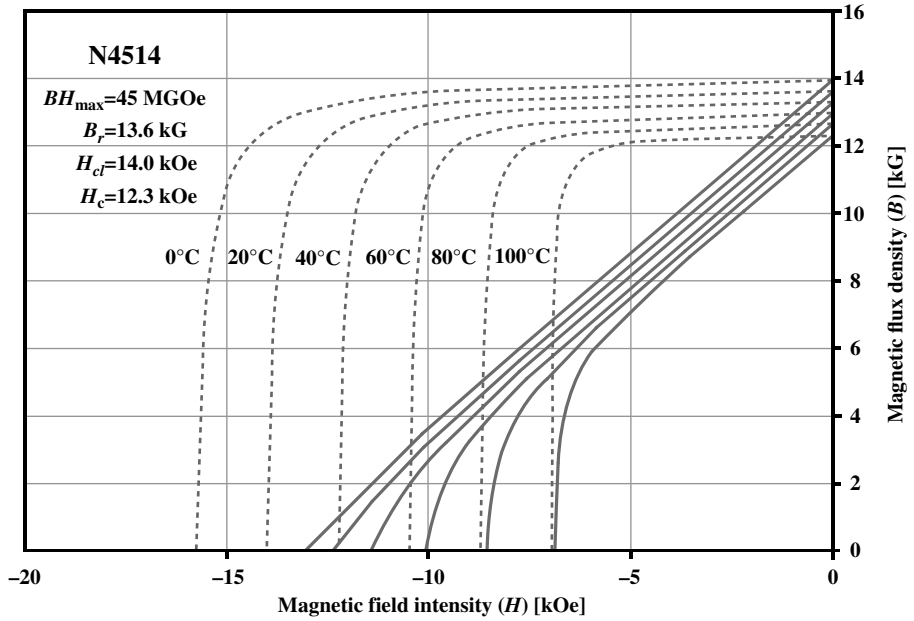

Figure 1.10 Intrinsic and normal *BH* curves of NdFeB magnet at different temperatures.

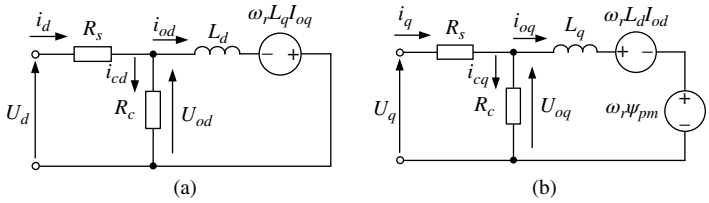

Figure 1.11 *dq*-axis equivalent circuits of PMSM: (a) *d*-axis and (b) *q*-axis.

decreases rapidly, which will cause irreversible demagnetization. Meanwhile, with the increasing temperature in the NeFeB magnets, both the remanence and the coercivity decrease with the rise in temperature, which will deteriorate the output torque and the demagnetization withstand capability, respectively.

Meanwhile, the temperature dependencies of the stator resistance and the rotor flux linkage are also widely used as thermal indicators to monitor thermal conditions indirectly. The detailed applications of condition monitoring will be introduced in Chapter 11.

1.3.2.3 Influence of Iron Loss

As previously mentioned, iron loss is not considered in an ideal PMSM model, but it does influence the flux linkage and output torque capability. Furthermore, the modelling of iron loss becomes critical when the machine is operated at high speed, low flux mode, or at variable speed [35]. The widely used PMSM equivalent circuit accounting for iron losses [36, 37] is presented in Figure 1.11, where it is assumed that the iron loss resistance R_c is greater than the product of the *dq*-axis reactances, i.e., $\omega_r^2 L_d L_q$, and the winding resistance R_s.

$$\frac{\omega_r^2 L_d L_q}{R_c^2} \ll 1 \text{ and } \frac{R_s}{R_c} \ll 1 \tag{1.20}$$

Therefore, the steady-state equations are as follows:

$$\begin{bmatrix} u_d \\ u_q \end{bmatrix} = \begin{bmatrix} R_s + \dfrac{\omega_r^2 L_d L_q}{R_c} & -\omega_r L_q \\ \omega_r L_d & R_s + \dfrac{\omega_r^2 L_d L_q}{R_c} \end{bmatrix} \begin{bmatrix} i_d \\ i_q \end{bmatrix} + \begin{bmatrix} \dfrac{\omega_r^2 L_q \psi_{pm}}{R_c} \\ \omega_r \psi_{pm} \end{bmatrix} \tag{1.21}$$

As can be seen, in the equivalent circuits, the iron loss is represented by a parallel connected iron loss resistance $R_c = \omega^2 L_d L_q / R_c$ in the stator circuit, which is a function of the magnetic flux and the electrical frequency. Thus, the output torque is strictly proportional to the magnetizing current. The magnetizing current is indirectly calculated based on the line current and the iron loss resistance.

1.4 Drives and Control Strategies

1.4.1 Drive System of PMSM

The schematic diagram of an electrical drive system for PMSM, including a voltage source inverter (VSI), a PMSM, and a control unit, is shown in Figure 1.12a and b. The control strategies play a critical role for PMSM drive systems and should achieve the following performance, e.g., high efficiency, lower torque ripple, wide speed controllability, fast dynamic response, high robustness and reliability, as well as ensuring system stability. For PMSMs, the phase currents need to be precisely controlled,

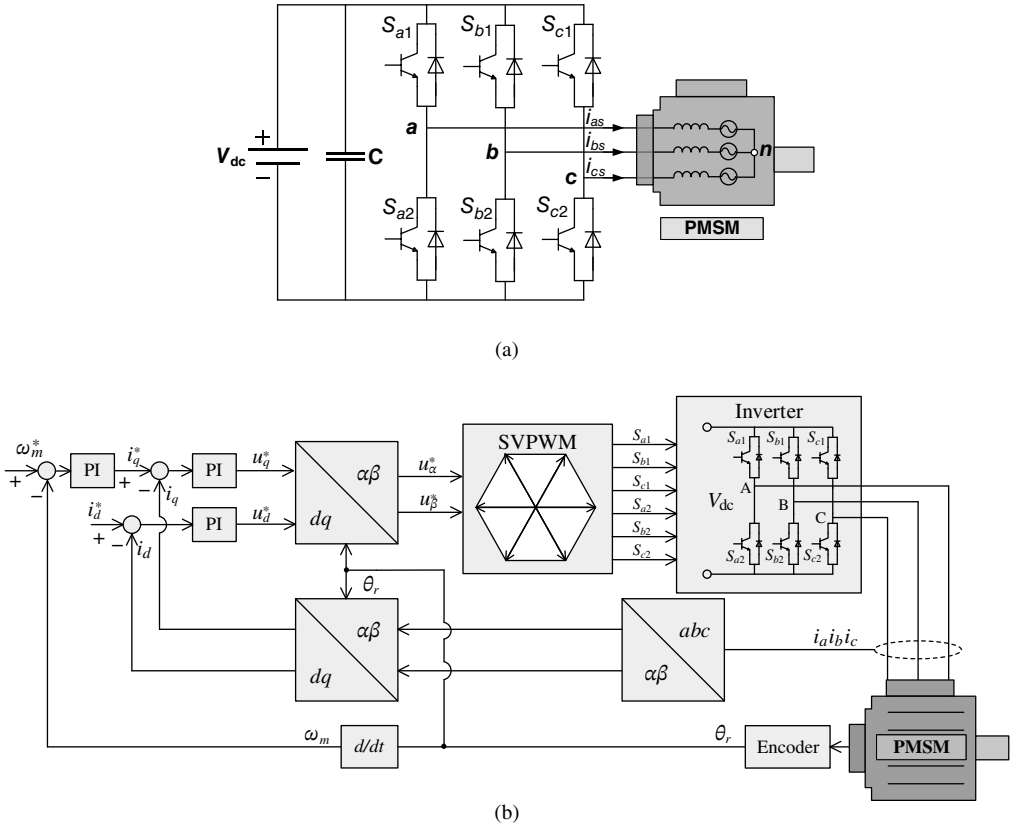

Figure 1.12 Schematic diagram of an electrical drive system for PMSM: (a) VSI-based three-phase PMSM drive system and (b) FOC system.

which can be achieved by employing space vector pulse width modulation (SVPWM), and high performance can be achieved by employing control methods in the controller, e.g., FOC, DTC, and MPC. The most popular control method is FOC, as shown in Figure 1.12.

FOC was first proposed in the 1970s and utilizes a similar control concept as for a dc motor. For PMSMs, the three-phase alternating current (ac) currents are decomposed into two orthogonal components in the rotating reference frame, i.e., the dc i_d and the quadrature current i_q, which are used to control the flux and torque separately. The relevant Park and Clarke transformations have been introduced in Section 1.3.1. In the FOC system, the accurate rotor position must be known and is usually obtained by using either a hardware rotor position sensor such as a resolver or encoder or software-based rotor position sensorless techniques [9]. In addition, two proportional–integral (PI) regulators are used to control both components of the current vector separately, where the accurate machine parameters are essential to determine the current vector and the PI constants for the regulators of both current and speed loops.

1.4.2 Space Vector Pulse Width Modulation

A three-phase VSI is used to provide variable voltage and frequency supply. PWM techniques have been studied extensively in the last few decades, and the SVPWM is most popular due to its high utilization of dc-link voltage and low harmonic distortion [38].

The three numbers for each voltage vector in Figure 1.13 represent the switching states of the three legs of the VSI (Figure 1.12a). To avoid the short circuit, the upper and lower switches in one leg work in the complementary mode with a dead time. Therefore, if the upper switch is on and the lower switch is off, the value of the switching state is "1," and if the upper switch is off and the lower switch is on, the value of the switching state is "0." In the SVPWM, there are six non-zero vectors (100, 110, 010, 011, 001, and 101) and two zero vectors (000 and 111). The whole voltage plane is evenly divided into six sectors by the non-zero voltage vectors, as presented in Figure 1.13, and the three-phase voltages $u_{a,b,c}$ and their corresponding space vectors are summarized in Table 1.2. The sinusoidal reference space vector follows a circular trajectory within the hexagon, and the maximum output phase voltage $u^*_{\text{s,max}}$ achieved by applying SVPWM is $\sqrt{3}/3V_{dc}$, where V_{dc} is the dc bus voltage.

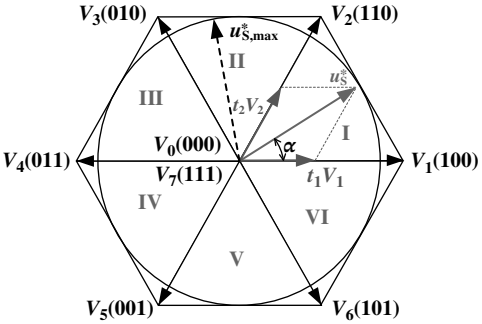

Figure 1.13 Phasor representation of eight basic space vectors.

Therefore, any voltage can be represented by two adjacent fundamental vectors together with zero vectors, and its amplitude is adjusted by the active durations of those fundamental vectors in a sampling period T_s. Taking the voltage vector reference u_s^* in Sector I as an example, Figure 1.13, the active durations (t_1, t_2, and t_0) of space vectors $\boldsymbol{V}_1$, $\boldsymbol{V}_2$, and $\boldsymbol{V}_0$ can be calculated as follows:

$$t_1 = \frac{u_s^*}{V_1}\frac{\sin(\pi/3 - \alpha)}{\sin(2\pi/3)} \tag{1.22a}$$

$$t_2 = \frac{u_s^*}{V_2}\frac{\sin(\alpha)}{\sin(2\pi/3)} \tag{1.22b}$$

$$t_0 = T_s - t_1 - t_2 \tag{1.22c}$$

where V_1 and V_2 are the amplitudes of voltage vectors, i.e.,$V_1 = V_2 = 2/3\ V_{dc}$. α is the angle of voltage vector reference.

Table 1.2 Correlation between voltages and corresponding space vectors.

Vector	Switching pattern	Phase voltage/V_{dc}			Line voltage/V_{dc}		
	$S_aS_bS_c$	u_a	u_b	u_c	u_{ab}	u_{bc}	u_{ca}
$\boldsymbol{V_0}$	000	0	0	0	0	0	0
$\boldsymbol{V_1}$	100	2/3	−1/3	−1/3	1	0	−1
$\boldsymbol{V_2}$	110	1/3	1/3	−2/3	0	1	−1
$\boldsymbol{V_3}$	010	−1/3	2/3	−1/3	−1	1	0
$\boldsymbol{V_4}$	011	−2/3	1/3	1/3	−1	0	1
$\boldsymbol{V_5}$	001	−1/3	−1/3	2/3	0	−1	1
$\boldsymbol{V_6}$	101	1/3	−2/3	1/3	1	−1	0
$\boldsymbol{V_7}$	111	0	0	0	0	0	0

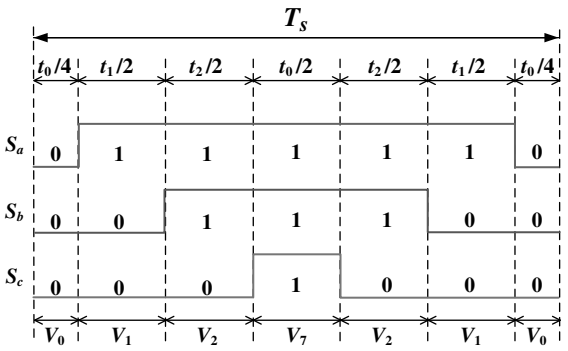

Figure 1.14 Switching states and gate signals within one sampling period in Sector I.

It is well-known that each inverter leg should change only once between 0 and 1 in one switching period to minimize switching loss [39]. Thus, this switching pattern can be achieved by applying the zero vectors followed by two active state vectors in a half-switching period, and then, the switching pattern is repeated in the next half-switching period. Figure 1.14 depicts the switching states within one sampling period in Sector I and the gate signals for each phase leg of the inverter.

In practice, to avoid damage to the power switching devices caused by the short circuit, a proper length of time delay, i.e., dead time, must be performed between the turn-on signal for one power switching device and the corresponding turn-off signal for the other power switching device in the same leg of the inverter. However, the introduced dead-time will cause a difference between the commanded and actual voltages, which will result in the distortions of output voltages and currents. To date, the compensation of dead-time voltage distortion [40, 41], together with the voltage distortions caused by the non-ideal characteristic of the switching device [42, 43], have been extensively developed. The detailed introduction of the influence of VSI non-linearity on the electrical parameter identification and the identification of VSI non-linearity will be described in Chapters 2 and 3, respectively.

1.5 Outline of Parameter Estimation Techniques

The state-of-the-art offline and online parameter estimation methods are outlined in Figure 1.15, and a comprehensive literature review (up to 2022) can be found in Ref. [19]. In this section, both offline and online parameter estimation methods are only briefly highlighted, as they will be comprehensively described later in this book.

1.5.1 Offline Parameter Estimation

The FEA is the most common offline method to estimate PMSM parameters but requires detailed knowledge of geometric and material information. It is widely reported that FEA can be used to calculate a rotor flux linkage map and incremental/apparent *dq*-axis inductances accounting for magnetic saturation and cross-coupling. An example of using FEA to analyse the electromagnetic performance of PMSM is presented in Appendix A. However, sometimes, FEA methods [30, 31] are limited since some material properties are unknown or not completely acquirable. Hence, offline experimental estimation methods have been extensively developed in the last few decades. Some methods are listed in the following.

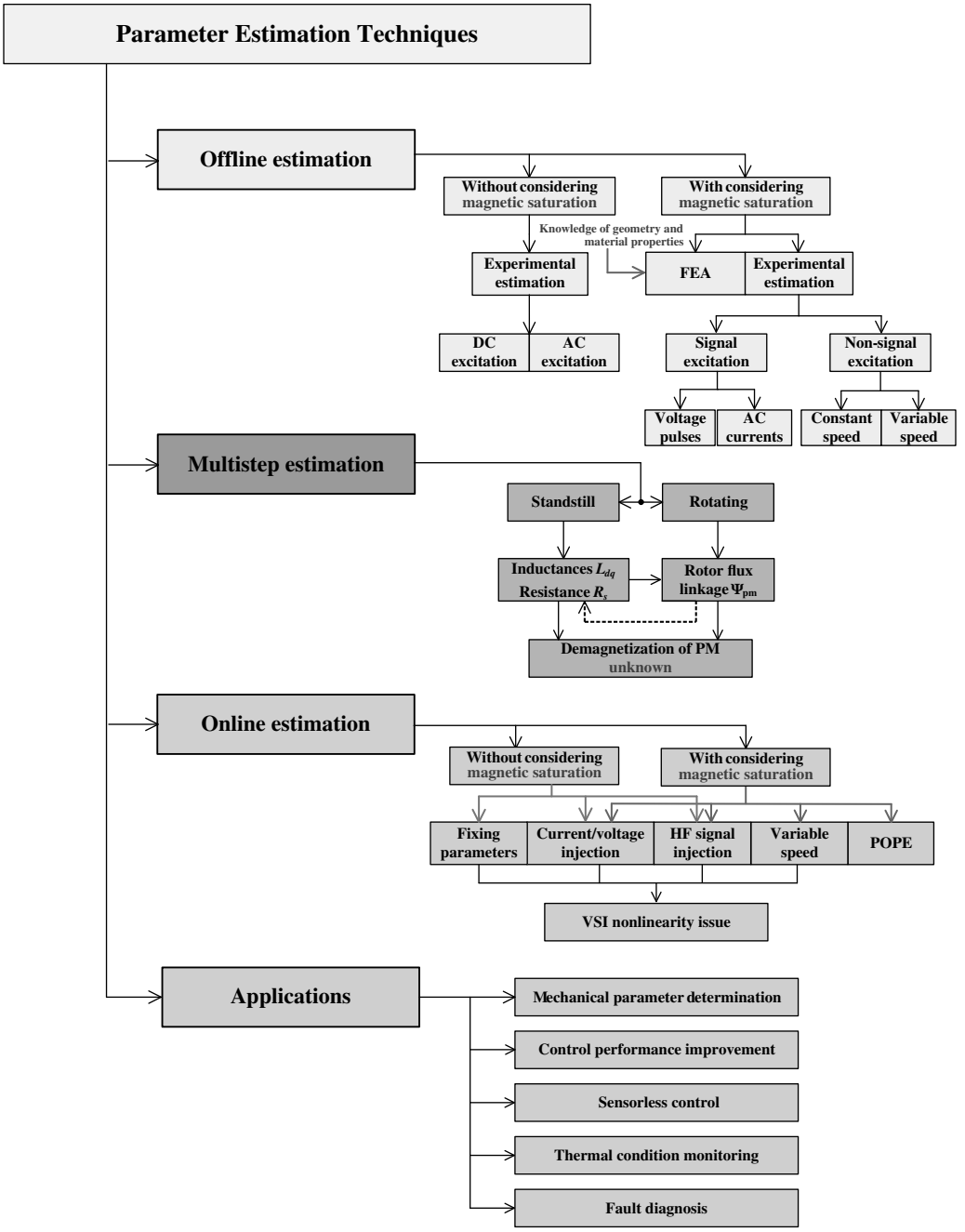

Figure 1.15 Overview of parameter estimation techniques.

1. Voltage excitation [44].
2. Magnetic model estimation:
   a. *dq*-axis voltage pulse injection [45].
   b. Fast Fourier transform (FFT) analysis [46].

c. AC signal excitation [3, 47].
d. Estimation under constant speed [10].
e. Estimation under variable speed [48, 49].

According to the time constant at the transient state, the step dc voltage excitation tests at a standstill in Ref. [44] are used to predict apparent inductance, but they cannot determine the rotor flux linkage or accurately consider the magnetic saturation effect. To identify dq-axis flux linkages and incremental inductances, the voltage pulses are applied to the d-axis and q-axis in turn while the other axis current remains constant [45]. Accounting for self- and cross-saturation effects, the dq-axis flux linkages are estimated by using the FFT method in Ref. [46] based on the measured dq-axis currents at constant rotor speed, and then, the dq-axis incremental inductances are calculated by the partial derivatives of dq-axis flux linkages with respect to currents. Besides, ac signal excitations are employed to estimate apparent [3] and incremental inductances [47], respectively, where the dc bias point sets the magnetic operating point in Ref. [47], and induced voltages and internal load angles are measured in Ref. [3]. Moreover, the magnetic models are estimated based on the FOC schemes at constant [10] and at variable speed [48, 49]. Specifically, an additional voltage measurement circuit is required in Ref. [10]. The variations of stator resistance and VSI-caused distorted voltage is determined at a standstill [48]. The dq-axis flux-linkage map is modelled as second-order polynomials under variable speed control [49]. It should be mentioned that the estimated dq-axis flux linkages can derive both incremental and apparent inductances based on Eqs. (1.15) and (1.16). However, the values of two types of inductances may be different due to magnetic saturation, and the above papers select either incremental or apparent inductance. In addition to the direct calculation by means of inductance definitions, the apparent inductances can also be estimated by utilizing the analysis of a phasor diagram [2] or the time constant of the armature winding circuit [25]. Besides, the multi-step estimation utilizes the acquirable parameters, e.g., stator resistance and distorted voltage drop, at standstill, and then, the rotor flux linkage and the stator apparent inductances can be estimated in the operating state [50–52]. Nevertheless, it cannot accurately track online parameter variations due to neglecting the magnet temperature rise and the core loss.

1.5.2 Online Parameter Estimation

Without relying on the nominal values/offline measurement, the online estimation methods are conducted during operation based on the available input and output measured quantities, i.e., current (i), voltage (v), and rotor speed (ω_r). Generally, the online parameter estimation process is carried out under sensored and sensorless control of the PMSM drive system. Both the electrical and mechanical parameters can be estimated by utilizing the various estimation algorithms and the measured quantities. The schematic diagram of online parameter estimation is shown in Figure 1.16, where $\Delta\omega_r$, Δi_d, Δu_d, and $\pm\Delta\theta_p$ are the variables of rotor speed, injected d-axis current and voltage, as well as the position offsets.

The general issues in online parameter estimation, including the rank-deficient problem, the VSI non-linearity, and the influence of signal injection, must be addressed first. To ensure the full-rank estimation schemes, the PMSMs usually need to be excited by one or more additional sets of signals, and the state-of-the-art methods include the injections of currents, voltages, HF signals, and rotor position offsets, along with intentionally changing the rotor speed. Although the online parameter estimation techniques incorporate high levels of computational efficiency, with the improvement of the computing capability of the processor, some AI or modern control theory-based algorithms have

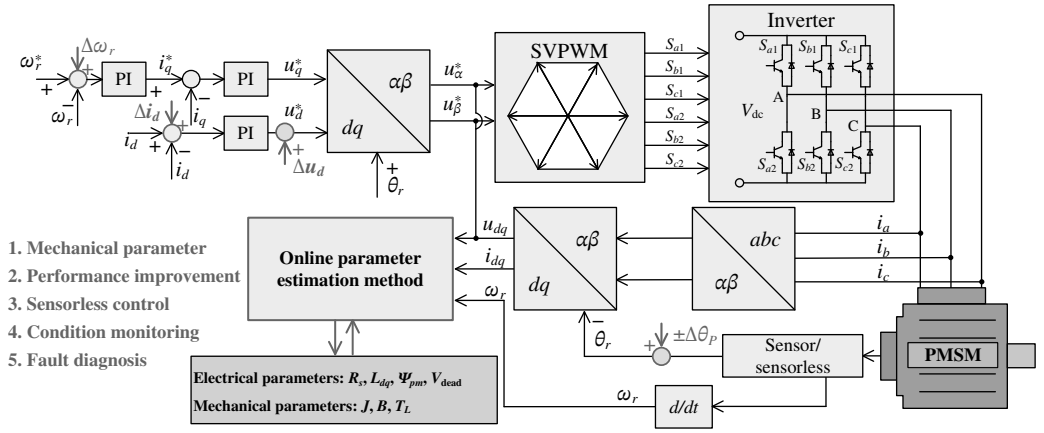

Figure 1.16 Schematic diagram of online parameter estimation.

been applied. Most online methods are concerned with the apparent inductance estimation since the terms of time derivation of *dq*-axis flux linkages are cancelled in the steady-state equation. Besides, the incremental inductances are also important for HF signal injection-based sensorless rotor position estimation, particularly at zero and low speed [9].

The main offline and online modelling techniques, including HF signal injection, will be illustrated later in this book in greater detail.

1.6 Scope of This Book

This book provides a comprehensive resource on the basic and state-of-the-art online and offline parameter estimation techniques for PMSMs, as summarized in Figure 1.17.

It starts with a brief description of PMSMs and drives and then introduces the basic parameters and estimation techniques in Chapter 1 and the issues in parameter estimation in Chapter 2, such as rank deficiency and non-linearity of inverter. It is followed by various online parameter estimation techniques based on rotor position sensored operation, including those (a) with the aid of thermocouples in the stator windings in Chapter 3, (b) based on current/voltage injections in Chapter 4, and (c) based on the position offset injection in Chapter 5, under constant and variable speeds and/or torque in Chapter 6. The effect of magnetic saturation and the cross-coupling effect in PMSMs, along with the corresponding parameter estimation methods, are reported in Chapter 7. Offline parameter estimation by signal injection at standstill and by multi-step methods is also described in Chapter 8. In addition, three different techniques for estimating mechanical parameters are described in Chapter 9. The book also introduces many modern control theory-based parameter estimation techniques, including recursive least squares, Kalman filter, model reference adaptive system, Adaline neural network, gradient-based methods, particle swarm optimization, and genetic algorithm in Chapter 10. Finally, applications of parameter estimation techniques for (a) improvement of control performance, (b) sensorless control, (c) thermal condition monitoring, and (d) fault diagnosis are presented in Chapter 11. The finite element method for calculating winding inductances is given in the appendix and the classic methods for estimating and testing the parameters of PMSMs are embodied in the main body for comparison.

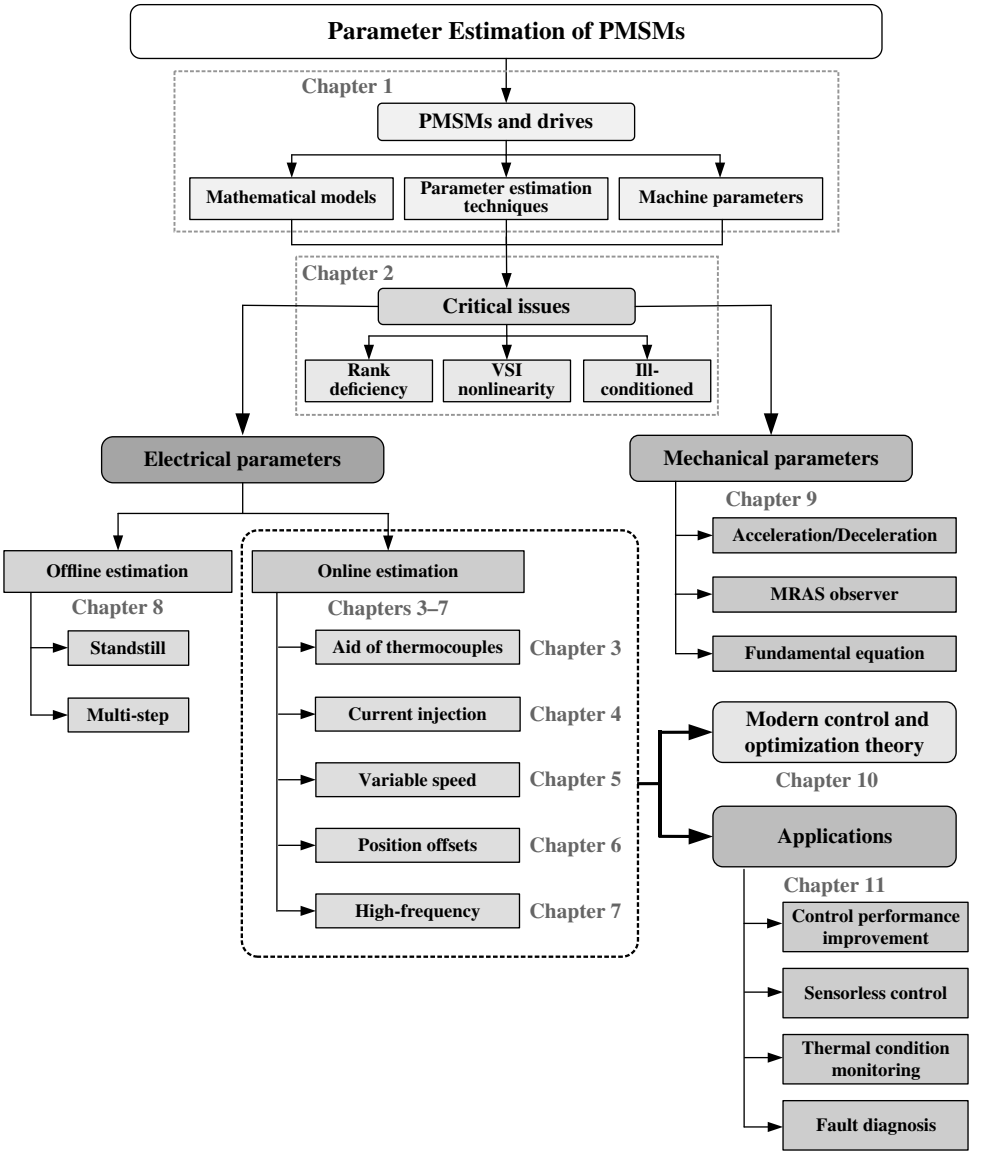

Figure 1.17 Outline of the book.

References

1 US Energy Information Administration, "Manufacturing Energy Consumption Survey." Energy Efficiency Indicators, 2020.

2 B. Chalmers, S. Hamed, and G. Baines, "Parameters and performance of a high-field permanent-magnet synchronous motor for variable-frequency operation," *IEE Proc. B*, vol. 132, no. 3, p. 117, May 1985.

3 B. Stumberger, B. Kreca, and B. Hribernik, "Determination of parameters of synchronous motor with permanent magnets from measurement of load conditions," *IEEE Trans. Energy Convers*, vol. 14, no. 4, pp. 1413–1416, Dec. 1999.

4 F. Fernandez-Bernal, A. Garcia-Cerrada, and R. Faure, "Determination of parameters in interior permanent-magnet synchronous motors with iron losses without torque measurement," *IEEE Trans. Ind. Appl.*, vol. 37, no. 5, pp. 1265–1272, Sept./Oct. 2001.

5 S.K. Sul, Control of Electric Machine Drive Systems. New Jersey: Wiley, 2011.

6 S. Li and Z. Liu, "Adaptive speed control for permanent-magnet synchronous motor system with variations of load inertia," *IEEE Trans. Ind. Electron*, vol. 56, no. 8, pp. 3050–3059, Aug. 2009.

7 K. Liu, "Research on the online multi-parameter identification of permanent magnet synchronous machines," PhD dissertation, Hunan Univ., Changsha, China, 2010.

8 J. Ziegler and N. Nichols, "Optimum settings for automatic controllers," *J. Fluids Eng.*, vol. 64, no. 8, pp. 759–765, 1942.

9 Z. Q. Zhu and X. M. Wu, *Sensorless Control of Permanent Magnet Synchronous Machine Drives*. New York: Wiley and IEEE Press, 2023.

10 E. Armando, R. Bojoi, P. Guglielmi, G. Pellegrino, and M. Pastorelli, "Experimental identification of the magnetic model of synchronous machines," *IEEE Trans. Ind. Appl.*, vol. 49, no. 5, pp. 2116–2125, Sept./Oct. 2013.

11 Y. Inoue, Y. Kawaguchi, S. Morimoto, and M. Sanada, "Performance improvement of sensorless IPMSM drives in a low-speed region using online parameter identification," *IEEE Trans. Ind. Appl.*, vol. 47, no. 2, pp. 798–804, Mar./Apr. 2011.

12 Z. Q. Zhu, P. Wang, N. M. A. Freire, Z. Azar, and X. Wu, "A novel rotor position-offset injection-based online parameter estimation of sensorless controlled surface-mounted PMSMs," *IEEE Trans. Energy Convers.*, vol. 39, no. 3, pp. 1930–1946, Sept. 2024.

13 Y. Li, Z. Q. Zhu, D. Howe, C. M. Bingham, and D. A. Stone, "Improved rotor-position estimation by signal injection in brushless AC motors, accounting for cross-coupling magnetic saturation," *IEEE Trans. Ind. Appl.*, vol. 45, no. 5, pp. 1843–1850, Sept./Oct. 2009.

14 D. D. Reigosa, F. Briz, P. García, J. M. Guerrero, and M. W. Degner, "Magnet temperature estimation in surface PM machines using high-frequency signal injection," *IEEE Trans. Ind. Appl.*, vol. 46, no. 4, pp. 1468–1475, July/Aug. 2010.

15 S. Wilson, P. Stewart, and B. Taylor, "Methods of resistance estimation in permanent magnet synchronous motors for real-time thermal management," *IEEE Trans. Energy Convers.*, vol. 25, no. 3, pp. 698–707, Sept. 2010.

16 K. Liu, "Novel techniques for parameter estimation of permanent magnet synchronous machines," PhD dissertation, University of Sheffield, Sheffield, U.K., Dec. 2013.

17 D. Liang, "Critical temperature estimation for permanent magnet synchronous machines," PhD dissertation, University of Sheffield, Sheffield, U.K., Feb. 2022.

18 Z. Q. Zhu and D. Liang, "Perspective of thermal analysis and management for permanent magnet machines, with particular reference to hotspot temperatures," *Energies*, vol. 15, no. 21, pp. 1–53, Nov. 2022.

19 Z. Q. Zhu, D. Liang, and K. Liu, "Online parameter estimation for permanent magnet synchronous machines: an overview," *IEEE Access*, vol. 9, pp. 59059–59084, 2021.

20 A. Binder, T. Schneider, and M. Klohr, "Fixation of buried and surface-mounted magnets in high-speed permanent-magnet synchronous machines," *IEEE Trans. Ind. Appl.*, vol. 42, no. 4, pp. 1031–1037, Jul./Aug. 2006.

21 S. Morimoto, M. Sanada, and Y. Takeda, "Wide-speed operation of interior permanent magnet synchronous motors with high-performance current regulator," *IEEE Trans. Ind. Appl.*, vol. 30, no. 4, pp. 920–926, Jul./Aug. 1994.

22 Y. Sato, S. Ishikawa, T. Okubo, M. Abe, and K. Tamai, "Development of high response motor and inverter system for the Nissan LEAF electric vehicle," SAE Technical Paper, 2011-01-0350, 2011.

23 M. Kamiya, "Development of traction drive motors for the Toyota hybrid system," *IEEJ Trans. Ind. Appl.*, vol. 126, no. 4, pp. 473–479, 2006.

24 A. E. Fitzgerald, C. Kingsley, and S. D. Umans, Electric Machinery. New York: McGraw-Hill, 1989.

25 Y. S. Chen, "Motor topologies and control strategies for permanent magnet brushless AC drives," Ph.D. dissertation, Univ. Sheffield, U.K., 1999.

26 A. M. El-Serafi, A. S. Abdallah, M. K. El-Sherbiny, and E. H. Badawy, "Experimental study of the saturation and the cross-magnetizing phenomenon in saturated synchronous machines," *IEEE Trans. Energy Convers.*, vol. 3, no. 4, pp. 815–823, Dec. 1988.

27 A. M. El-Serafi and J. Wu, "Determination of the parameters representing the cross-magnetizing effect in saturated synchronous machines," *IEEE Trans. Energy Convers.*, vol. 8, no. 3, pp. 333–342, Sept. 1993.

28 Z. Azar, Z.Q. Zhu, and G. Ombach, "Influence of electric loading and magnetic saturation on cogging torque, back-EMF and torque ripple of PM machines," *IEEE Trans. Magn.*, vol. 48, no. 10, pp. 2650–2658, Oct. 2012.

29 W. Xu and R. D. Lorenz, "High-frequency injection-based stator flux linkage and torque estimation for DB-DTFC implementation on IPMSMs considering cross-saturation effects," *IEEE Trans. Ind. Appl.*, vol. 50, no. 6, pp. 3805–3815, Nov./Dec. 2014.

30 N. A. Demerdash, T. M. Hijazi, and A. A. Arkadan, "Computation of winding inductances of permanent magnet brushless DC motors with damper windings by energy perturbation," *IEEE Trans. Energy Convers.*, vol. 3, no. 3, pp. 705–713, Sept. 1988.

31 T. W. Nehl, F. A. Fouad, and N. A. Demerdash, "Determination of saturated values of rotating machinery incremental and apparent inductances by an energy perturbation method," *IEEE Power Eng. Rev.*, vol. PER-2, no. 12, pp. 28–29, Dec. 1982.

32 N. A. Demerdash and T. W. Nehl, "Electric machinery parameters and torques by current and energy perturbations from field computations. I. Theory and formulation," *IEEE Trans. Energy Convers.*, vol. 14, no. 4, pp. 1507–1513, Dec. 1999.

33 S. Liu and G. Kuhl, "Temperature coefficients of rare earth permanent magnets," *IEEE Trans. Magn.*, vol. 35, no. 5, pp. 3271–3273, Sept. 1999.

34 *ND Magnets-N4514*, Dexter Magnet Technologies, [Online]. Available https://www.dextermag.com/products/permanent-magnets/nd-magnets-n4514/.

35 M. Popescu, D. G. Dorrell, and D. M. Ionel, "A study of the engineering calculations for iron losses in 3-phase AC motor models," *IECON 2007 – 33rd Ann. Conf. IEEE Ind. Electron. Soc.*, 2007, pp. 169–174.

36 N. Urasaki, T. Senjyu, and K. Uezato, "A novel calculation method for iron loss resistance suitable in modeling permanent-magnet synchronous motors," *IEEE Trans. Energy Convers.*, vol. 18, no. 1, pp. 41–47, March 2003.

37 S. Morimoto, Y. Tong, Y. Takeda, and T. Hirasa, "Loss minimization control of permanent magnet synchronous motor drives," *IEEE Trans. Ind. Electron.*, vol. 41, no. 5, pp. 511–517, Oct. 1994.

38 D Holmes and T. Lipo, *Pulse width modulation for power converters*. Hoboken, NJ: John Wiley, *2003*.

39 S. Bowes and Y. Lai, "The relationship between space-vector modulation and regular-sampled PWM," *IEEE Trans. Ind. Electron*., vol. 44, no. 5, pp. 670–679, Oct. 1997.

40 Y. Murai, T. Watanabe, and H. Iwasaki, "Waveform distortion and correction circuit for PWM inverters with switching lag-times," *IEEE Trans. Ind. Appl*., vol. IA-23, no. 5, pp. 881–886, Sept. 1987.

41 S. Jeong and M. Park, "The analysis and compensation of dead-time effects in PWM inverters," *IEEE Trans. Ind. Electron*., vol. 38, no. 2, pp. 108–114, April 1991.

42 J. Choi and S. K. Sul, "Inverter output voltage synthesis using novel dead time compensation," *IEEE Trans. Power Electron*., vol. 11, no. 2, pp. 221–227, March 1996.

43 N. Urasaki, T. Senjyu, K. Uezato, and T. Funabashi, "An adaptive dead-time compensation strategy for voltage source inverter fed motor drives," *IEEE Trans. Power Electron*., vol. 20, no. 5, pp. 1150–1160, Sept. 2005.

44 S. Weisgerber, A. Proca, and A. Keyhani, "Estimation of permanent magnet motor parameters," In *Proc. IEEE Ind. Appl. Soc. Annu. Meeting*, 1997, vol. 1, pp. 29–34.

45 B. Stumberger, G. Stumberger, D. Dolinar, A. Hamler, and M. Trlep, "Evaluation of saturation and cross-magnetization effects in interior permanent-magnet synchronous motor," *IEEE Trans. Ind. Appl*., vol. 39, no. 5, pp. 1264–1271, Sept./Oct. 2003.

46 K. M. Rahman and S. Hiti, "Identification of machine parameters of a synchronous motor," *IEEE Trans. Ind. Appl*., vol. 41, no. 2, pp. 557–565, Mar./Apr. 2005.

47 S. A. Odhano, R. Bojoi, S. G. Rosu, and A. Tenconi, "Identification of the magnetic model of permanent-magnet synchronous machines using DC-biased low-frequency AC signal injection," *IEEE Trans. Ind. Appl*., vol. 51, no. 4, pp. 3208–3215, Jul./Aug. 2015.

48 G. Pellegrino, B. Boazzo, and T. M. Jahns, "Magnetic model self-identification for PM synchronous machine drives," *IEEE Trans. Ind. Appl*., vol. 51, no. 3, pp. 2246–2254, May/Jun. 2015.

49 K. Liu, J. Feng, S. Guo, L. Xiao, and Z.Q. Zhu, "Identification of flux linkage map of permanent magnet synchronous machines under uncertain circuit resistance and inverter nonlinearity," *IEEE Trans. Ind. Informat*., vol. 14, no. 2, pp. 556–568, Feb. 2018.

50 M. Rashed, P. Macconnell, A. Stronach, and P. Acarnley, "Sensorless indirect-rotor-field-orientation speed control of a permanent-magnet synchronous motor with stator-resistance estimation," *IEEE Trans. Ind. Electron*., vol. 54, no. 3, pp. 1664–1675, Jun. 2007.

51 S. Morimoto, M. Sanada, and Y. Yakeda, "Mechanical sensorless drives of IPMSM with online parameter identification," *IEEE Trans. Ind. Appl*., vol. 42, no. 5, pp. 1241–1248, Sep./Oct. 2006.

52 S. Lee, "Closed-loop estimation of permanent magnet synchronous motor parameters by PI controller gain tuning," *IEEE Trans. Energy Convers*., vol. 21, no. 4, pp. 863–870, Dec. 2006.